Nanoscale

ROYAL SOCIETY OF CHEMISTRY

COMMUNICATION

View Article Online
View Journal | View Issue

Cite this: *Nanoscale*, 2025, **17**, 7030

Received 8th November 2024,
Accepted 17th February 2025

DOI: 10.1039/d4nr04655b

rsc.li/nanoscale

Tungsten oxide nanocrystals doped with interstitial methylammonium cations†

Owen Kendall, [a] Lesly V. Melendez, [a] Merve Nur Guven Bicer, [a] Michael Wilms, [a] Joel van Embden, [a] Daniel E. Gómez, [a] Arrigo Calzolari, [b] Deborah Prezzi *[b] and Enrico Della Gaspera *[a]

Doping of semiconductor nanocrystals is a well-established process to impart new or enhanced functionalities to the host material. In this work we present the synthesis of colloidal WO_3 nanocrystals doped with interstitial methylammonium cations. The organic cations are located within the voids of the WO_3 cage and increase the charge carrier concentration. As a result, the nanocrystals exhibit intense surface plasmon resonances in the near infrared, comparable to those obtained for WO_3 "bronzes" doped with alkali metals. We confirm the successful incorporation of these novel organic dopants through a combined experimental and theoretical study. Furthermore, we demonstrate the ability to dope the nanocrystals with even larger cations including formamidinium, providing a pathway to obtaining WO_3 doped with bespoke organic cations that offer additional functionalities for use in optics, electronics and catalysis.

Degenerately doped semiconductors that exhibit a localized surface plasmon resonance (LSPR) have garnered significant attention for various applications, including electrochromic coatings, photothermal therapy, heat harvesters and (photo) catalysis.[1–3] Unlike noble metal nanocrystals (NCs), which typically exhibit bulk-like plasmonic resonances in the visible region of the electromagnetic spectrum,[4,5] doped semiconductors can display plasmonic absorptions in the near infrared (NIR) thanks to their lower free carrier concentrations.[1] As such, doped semiconductor NCs may play a crucial role in light harvesting applications such as photovoltaics and photocatalysis.[3] Moreover, while the plasmonic properties of noble metal NCs are primarily influenced by variations of the particle size and shape[4,6] and by alloying with other metals,[7] control of the plasmon absorption in doped semiconductors is mainly achieved by fine-tuning the dopant concentration, in addition to manipulating the size and shape of the NCs.[8–11]

Amongst the various degenerately doped metal oxides, oxygen-deficient tungsten oxide (WO_{3-x}) and interstitially doped tungsten bronzes (A_xWO_3) have received considerable attention due to their interesting optical and electronic properties. While stoichiometric tungsten trioxide (WO_3) is an intrinsic semiconductor and lacks plasmonic properties, off-stoichiometric compositions with oxygen deficiencies can introduce a high density of free electrons, usually compensated by a reduction in the oxidation state of tungsten, thereby triggering LSPR absorption.[12,13] Tungsten bronzes achieve their plasmonic behavior through interstitial doping of suitably sized monovalent cations, which occupy "voids" formed within the crystal lattice by the arrangement of the WO_6 octahedra. Doping of the hexagonal void is the most frequently observed, with cesium[14–16] and rubidium[17,18] being the most commonly studied dopants. The use of alternative inorganic cations has also been explored,[12,14,18–20] although again mostly focusing on alkali metals. Notably, some reports have demonstrated the successful incorporation of ammonium (NH_4^+) ions into the WO_3 crystal lattice,[13,21,22] giving rise to similar effects on the optical properties to those observed with conventional inorganic dopants. Very little research has been conducted so far on the incorporation of other organic cations as dopants within tungsten oxide systems, and only limited to bulk crystals.[23]

Herein, we demonstrate the doping of tungsten oxide NCs with large organic cations, specifically methylammonium (MA). By combining optical UV-Vis-NIR spectroscopy, X-ray diffraction (XRD) and transmission electron microscopy (TEM), we show the effect of MA^+ doping on the optical, morphological and structural properties of the NCs. Moreover, X-ray photoelectron spectroscopy (XPS) is utilized to confirm MA^+ insertion within the system. Finally, computational simulations are carried out to illustrate the similarities in the NCs electronic properties between MA and alkali metal doping, reinforcing the potential of organic cations as dopants in

[a]*School of Science, RMIT University, Melbourne, VIC 3000, Australia.*
E-mail: enrico.dellagaspera@rmit.edu.au
[b]*CNR-NANO Istituto Nanoscienze, Centro S3, I-41125 Modena, Italy.*
E-mail: deborah.prezzi@nano.cnr.it

†Electronic supplementary information (ESI) available: Experimental and computational details, additional XRD, TEM, XPS, UV-Vis and theoretical calculations. See DOI: https://doi.org/10.1039/d4nr04655b

these systems. As further proof of concept, we demonstrate the doping of WO_3 with even larger formamidinium (FA) cations, underscoring the versatility and robustness of the synthesis protocol.

The WO_3-based NCs were synthesized adapting literature methods with some modifications (see ESI† for details).[19] In brief, a solution of ammonium metatungstate in oleylamine containing varying amounts of methylammonium iodide (MAI) was degassed at 80 °C for 30 min in a round bottom flask connected to a Schlenk line. The solution was then heated to 250 °C under nitrogen and held at this temperature for 2 hours. Upon completion, the reaction was allowed to cool naturally, and the NCs were isolated *via* conventional precipitation and resuspension protocols. This synthesis method produces NCs of both undoped and MA-doped WO_{3-x}, as shown in Fig. 1.

Fig. 1a compares the XRD patterns of undoped (orange) and MA-doped (blue) WO_3 NCs, which both show features of a distorted cubic/monoclinic $WO_{2.72}$ crystal (see Fig. 1b for the ball-and-stick model, and also Fig. S1†). This result is expected, since the colloidal synthesis carried out in a mildly reducing solvent (oleylamine) is likely to produce oxygen-deficient NCs.[24] The diffraction peaks are quite broad, except the main peak centered at ~23.5° (corresponding to the (010) diffraction), suggesting strong anisotropy of the crystallites. Interestingly, no drastic changes occur to the crystal structure of the material with increased dopant loading, and this cubic/monoclinic phase is retained across all the doping levels tested (0–0.825 mmol MAI, Fig. S2†). This suggests that the MA^+ ion incorporation has negligible effects in terms of stress or strain on the surrounding WO_3 cage. A similar behavior is observed for WO_3 NCs doped with other alkali metals such as rubidium (Fig. S3†). This is, however, in contrast with cesium doping, which causes a change to either a cubic $(Cs_2O)_{0.44}WO_3$ or hexagonal phase (Fig. S4†). This is quite typical for Cs-doped WO_3 NCs, and the observed phase has been shown to be also dependent on the counterion of the cesium salt used.[2,11,14] Fig. 1c–j shows the TEM images of the NCs, with additional images also shown in Fig. S5 in the ESI.† As observed, undoped particles are highly crystalline and rod-shaped in nature, in agreement with the XRD results. From these observations, we can also deduce that these nanorods grow along the (010) direction. Size analysis of these particles results in average length and width values of 7.8 ± 1.8 nm and 1.5 ± 0.4 nm respectively, giving an aspect ratio (length/width) of ≈5.1. The addition of MA^+ as a dopant does not seem to affect the NC shape, which remains rod-like. However, a change in particle size is observed in presence of MA doping, with the average length of the NC increasing to 11.5 ± 3.0 nm, while the thickness remains unchanged at 1.6 ± 0.4 nm. This results in an aspect ratio of ≈7.3. Samples synthesized with different doping levels show a similar increase in aspect ratio, with the respective TEM images available in the ESI as Fig. S6.†

After discussing the structural and morphological properties of the NCs, we now move to elucidate their electronic structure and the bonding environment using XPS. Fig. 2a and b shows the W 4f regions for undoped WO_{3-x} and MA-doped WO_{3-x} NCs, while the O 1s region and the full survey are avail-

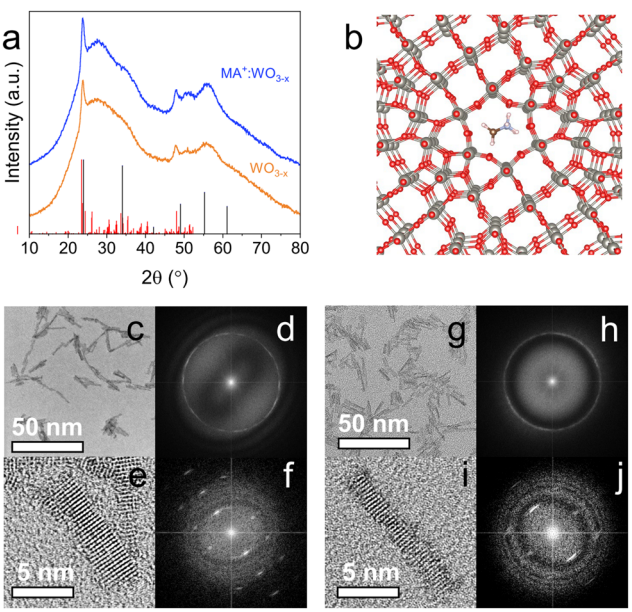

Fig. 1 (a) XRD patterns for undoped (orange) and MA-doped (blue) WO_{3-x} NCs. The reference peak positions for cubic WO_3 (black lines, ICDD: 41-0905) and monoclinic $WO_{2.72}$ (red lines, ICDD: 71-2450) tungsten oxide are shown at the bottom. (b) Schematic representation of the $WO_{2.72}$ crystal showing one MA^+ dopant (red = oxygen, grey = tungsten, brown = carbon, light blue = nitrogen). (c–j) TEM characterization of undoped (c–f) and MA-doped (g–j) NCs. The FFT images of both low- and high-resolution TEM images are presented on the right of the respective image.

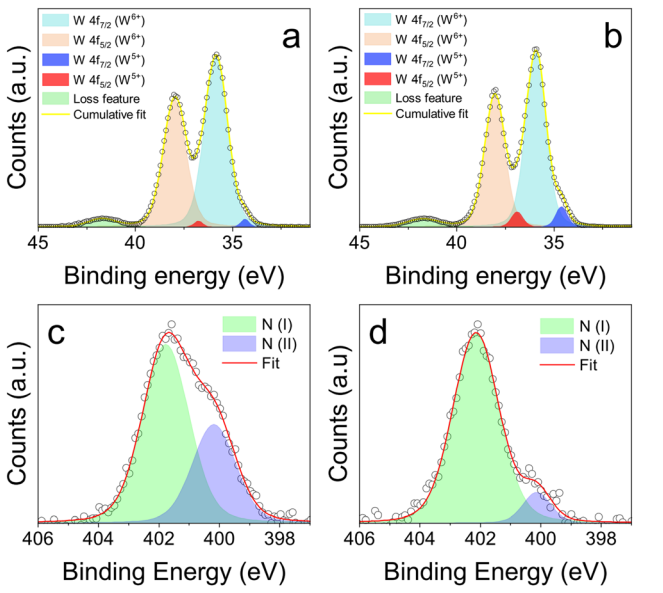

Fig. 2 (a and b) XPS spectra of the W 4f region of undoped (a) and MA^+ doped (b) WO_{3-x} NCs. (c and d) XPS spectra in the N 1s region for doped NCs before (c) and after (d) treatment with trifluoroacetic acid.

able in the ESI (Fig. S7 and S8†). Undoped WO_{3-x} NCs show a typical W 4f spectrum with two main peaks assigned to W 4f 7/2 and 5/2 components, located at 35.8 eV and 38.0 eV, respectively, with a spin orbit splitting of 2.2 eV (Fig. 2a). These components could be fitted with a single peak each, highlighting the presence of tungsten in the +6 oxidation state. However, careful peak fitting shows an additional doublet located at 34.4 eV and 36.7 eV, although very weak. This additional doublet has been ascribed to the W 4f 7/2 and 5/2 component of W^{5+} as a consequence of the off-stoichiometric nature of the undoped oxide. Here, a charge compensation mechanism takes place to counterbalance the presence of oxygen vacancies. An additional weak peak, located at ≈42 eV, has been attributed to a loss feature.[19,21] Similarly to undoped samples, MA-doped WO_{3-x} also shows the presence of tungsten in the +6 state, with W 4f 7/2 and 5/2 values of 35.8 eV and 38.0 eV respectively, as well as the loss feature peak at ≈42 eV (Fig. 2b). Interestingly, the doublet ascribed to W^{5+} is more intense in the doped samples. This confirms the successful doping with MA and the correspondingly larger charge compensation mechanism following the addition of interstitial dopants within WO_3.[13,19,21,25] This compositional effect is quantified in Fig. S9,† which shows the relationship between the amount of the MAI used in the synthesis, and the amount of W(v) detected from XPS (see also Table S1†). It can be clearly seen that the doped NCs show a higher fraction of reduced tungsten, consistent with the increased doping level. We note that the presence of ammonium dopants cannot be excluded due to the nature of the tungsten precursor, and as such the effective final doping is due to a combination of both MA^+ and ammonium cations.[13,21] The O 1s region of both undoped and doped NCs shows a single peak centered at ~531 eV and slightly asymmetric at higher binding energies, as routinely observed in metal oxides (Fig. S8†). Careful fitting of this peak shows the presence of multiple contributions, the most intense at lower binding energies being ascribed to W–O bonds, and others at higher binding energies arising from hydroxyls, and oxygen-containing organic contaminants.

To provide further evidence of the dopant incorporation, we focused on the N 1s region, that shows an asymmetric peak with two components, one at higher binding energy assigned to the R-NH_3^+ group of methylammonium, and one at lower binding energy assigned to the R-NH_2 of oleylamine, which is the surface ligand of the NCs. To confirm this assignment, we used trifluoroacetic acid (TFA) to strip the ligands from the NC surface, since TFA can protonate amines, facilitating their release.[26,27] As shown in Fig. 2c and d, the sample before and after TFA exposure shows the two components, centered at 402.0 eV and 400.1 eV. These values closely match literature reports of the N 1s of R-NH_3^+ groups and R-NH_2 groups, including methylammonium lead halide perovskites,[28,29] NH_4^+ doped WO_3 nanocrystals[13,21] and amine capped particles.[30,31] It is clear that the addition of TFA causes a decrease in the relative intensity of the low binding energy component (values reported in Table S2†), suggesting that surface amine ligands are removed, while intercalated MA cations are preserved. The core-level shift (CLS) prediction for the N 1s signal obtained from first principles density-functional theory (DFT) simulations show that methylammonium molecules within the WO_3 cage give rise to a contribution at 2.16 eV with respect to the reference position of the N 1s peak of the respective amine (CH_3NH_2).[32,33] This shift is consistent with our experimental observations and constitutes a further proof that methylammonium ions have been successfully incorporated within tungsten oxide NCs.

First principles DFT simulations were also carried out to investigate the effect of MA insertion on the electronic properties of tungsten oxide bulk material (see details in the ESI†). From the simulated density of states (DOS), we find that the effect of MA insertion into WO_3 is very similar to that of Cs, one of the most common dopants for tungsten bronzes (see Fig. S10†). This confirms the ability of organic cations to impart metallic behavior to tungsten oxide. Fig. 3a shows the DOS of stoichiometric hexagonal WO_3 (h-WO_3, grey shaded curve) as compared to that of undoped (orange line) and MA-doped (blue line) monoclinic $WO_{2.72}$ (also known as $W_{18}O_{49}$), one of the possible structures for the oxygen-deficient WO_{3-x}. In this instance, the metallic nature of $W_{18}O_{49}$ makes the doping effect less prominent, but still visible and very similar to what obtained for MA-doped h-WO_3 reported in the ESI.† Notably, the orientation of the MA cation within the WO_3 crystal has a negligible effect on the resulting electronic properties (Fig. S10†). Valence band XPS (Fig. 3b) confirms the electron degenerate nature of the synthesized NCs, showing the onset of the valence band for both doped and undoped NCs at ~3 eV. This indicates a Fermi level located 3 eV above the valence band edge. Considering a reported band gap for

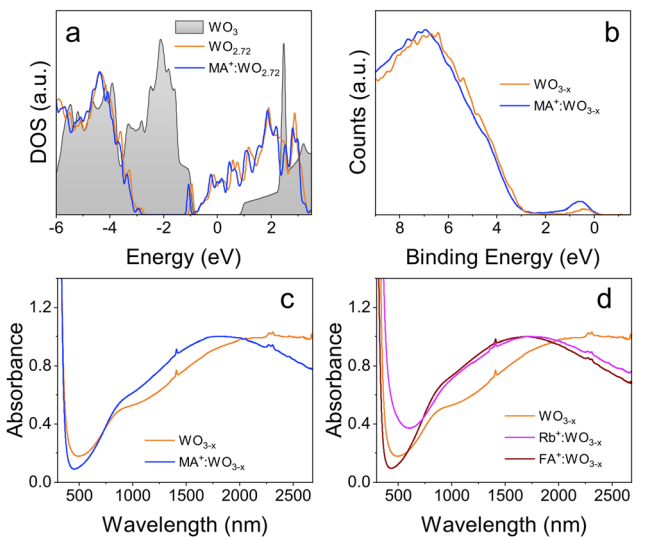

Fig. 3 (a) Density of states (DOS, E_F = 0) for stoichiometric WO_3 (grey), oxygen deficient $WO_{2.72}$ (orange), and MA-doped $WO_{2.72}$ (blue). (b) Valence band XPS spectra of undoped and MA-doped NCs. (c) Optical absorption spectra for undoped and MA-doped NCs. (d) Optical absorption spectra for Rb- and FA-doped NCs. The spectra have been normalized in intensity at the LSPR maximum.

WO_3 in the 2.7–3.0 eV range, these results confirm the metallic behavior of the NCs. Importantly, a peak located near the Fermi edge could be identified in both doped and undoped NCs, which has been attributed to the photoemission of electrons residing in the conduction band.[34–36] The addition of MA^+ dopants imparts a noticeable increase in the intensity of this peak, indicating an increase in the concentration of charge carriers. This again points towards the successful incorporation of the MA^+ ion within the WO_3 crystal.

One of the main effects of doping can be seen in the optical properties of the NCs, due to their LSPRs in the near infrared. As seen in Fig. 3c, undoped NCs show two distinct absorption features in the IR region, a shoulder centered at ~900 nm, and a broad peak detected at ~2300 nm. The fact that nominally undoped NCs show a LSPR as well is not surprising due to their sub-stoichiometric nature mentioned earlier.[24] Since TEM confirmed that the NCs are rod-shaped, it is believed that the LSPR feature at shorter wavelengths corresponds to the transverse plasmon mode, while the peak at longer wavelengths corresponds to the longitudinal mode. Doped NCs also display two absorption features in the NIR region. The first absorption feature is again a shoulder centered at ~900 nm, with negligible shift with respect to the undoped NCs. The second absorption feature however undergoes a marked blue shift with the addition of MA^+. This shift is progressively larger as more dopant is added to the NCs, with the absorption feature for the most doped samples shifting to <1800 nm, again pointing to an increase in free charge carriers. This blue shift was observed regardless of the increase in aspect ratio recorded for MA-doped samples, which would cause a red-shift of the LSPR peak for a fixed free electron density. This further indicates the presence of additional free charge carriers and, hence, the successful incorporation of MA^+ ions as interstitial dopants. Notably, while the spectra in Fig. 3 have been normalized at the plasmon peak, the raw spectra obtained from equally concentrated solutions show also an increase in intensity of the LSPR with doping, consistent again with the increase carrier density (Fig. S11†). The carrier concentration for undoped and doped NCs can be estimated based on the LSPR frequency and the nanoparticle aspect ratio (see ESI† for details).[37,38] The estimated electron density in doped NCs is more than double that of the undoped WO_{3-x} (6.6×10^{20} cm^{-3} compared to 2.6×10^{20} cm^{-3}), again corroborating the successful doping.

The most effective dopant incorporation occurs when adding 0.165 mmol MAI. If the amount of the dopant precursor is further increased, there is no clear benefit in terms of blue shift of the LSPR peak (Fig. S12†), suggesting a solubility limit of MA, and a potential detrimental effect (*e.g.* crystal distortions, phase segregation) if more dopant is added. For comparison, rubidium doped WO_3 nanocrystals were synthesized using RbI as a dopant source. Absorbance measurements show that WO_{3-x} NCs doped with MA^+ share very similar optical properties as Rb^+ doped WO_{3-x} (Fig. 3d). The ability to dope inorganic semiconductors with organic cations can provide new possibilities featuring novel dopants with tailored functionalities. To this extent, as a proof of concept we have conducted the synthesis of formamidinium (FA)-doped WO_{3-x} NCs, demonstrating the formation of crystalline tungsten oxide particles with enhanced plasmonic properties compared to undoped WO_{3-x}, and consistent with results obtained for MA- and Rb-doped WO_{3-x} (Fig. 3d and Fig. S13†). From one hand this confirms the robustness of the implemented synthesis approach; on the other hand, it points out the versatility of tungsten oxide to incorporate complex dopants, which is key to engineer and tailor new conductive (super)structures.

In conclusions, we have demonstrated the synthesis of a novel class of NCs based on WO_3 doped with interstitial organic cations using methylammonium as a case study. These dopants provide similar properties compared to conventional alkali metal dopants used in tungsten bronze NCs, while also offering further opportunities in view of the versatility of organic dopants. Therefore, this work opens a new avenue of research for doped tungsten oxide, with organic cations being able to provide additional functionalities that can be tailored by appropriately selecting the nature of the molecule chosen as dopant. This new class of dopants could be exploited beyond plasmonics, for example for simultaneously tailoring NC growth during synthesis and providing tunable LSPR to the NCs, or through the provision of additional functional groups (carboxylates, hydroxyls, thiols) and related reactive sites that could drive specific catalytic reactions.

Data availability

All relevant data are within the manuscript and the ESI.† Further clarification on data is available upon request from the authors.

Conflicts of interest

There are no conflicts to declare.

Acknowledgements

The Australian Research Council is acknowledged for financial support (DP220100020). The authors acknowledge the facilities and the technical assistance of the RMIT University's Microscopy and Microanalysis Facility (RMMF), as well as the CINECA award under the ISCRA initiative, for the availability of high-performance computing resources and support.

References

1 X. Liu and M. T. Swihart, *Chem. Soc. Rev.*, 2014, **43**, 3908–3920.
2 B. Z. Zydlewski, H.-C. Lu, H. Celio and D. J. Milliron, *J. Phys. Chem. C*, 2022, **126**, 14537–14546.

3 A. Agrawal, S. H. Cho, O. Zandi, S. Ghosh, R. W. Johns and D. J. Milliron, *Chem. Rev.*, 2018, **118**, 3121–3207.
4 K.-S. Lee and M. A. El-Sayed, *J. Phys. Chem. B*, 2006, **110**, 19220–19225.
5 A. Moores and F. Goettmann, *New J. Chem.*, 2006, **30**, 1121–1132.
6 E. Ringe, M. R. Langille, K. Sohn, J. Zhang, J. Huang, C. A. Mirkin, R. P. Van Duyne and L. D. Marks, *J. Phys. Chem. Lett.*, 2012, **3**, 1479–1483.
7 S. Link, Z. L. Wang and M. A. El-Sayed, *J. Phys. Chem. B*, 1999, **103**, 3529–3533.
8 Y. Cheref, F. Lochon, L. Daugas, C. Cleret de Langavant, É. Larquet, A. Baron, T. Gacoin and J. Kim, *Chem. Mater.*, 2022, **34**, 9795–9802.
9 P. Wainer, O. Kendall, A. Lamb, S. J. Barrow, A. Tricoli, D. E. Gómez, J. van Embden and E. Della Gaspera, *Chem. Mater.*, 2019, **31**, 9604–9613.
10 A. Agrawal, I. Kriegel and D. J. Milliron, *J. Phys. Chem. C*, 2015, **119**, 6227–6238.
11 T. M. Mattox, A. Bergerud, A. Agrawal and D. J. Milliron, *Chem. Mater.*, 2014, **26**, 1779–1784.
12 S. Heo, C. J. Dahlman, C. M. Staller, T. Jiang, A. Dolocan, B. A. Korgel and D. J. Milliron, *Nano Lett.*, 2020, **20**, 2072–2079.
13 R. Dören, B. Leibauer, M. A. Lange, E. Schechtel, L. Prädel, M. Panthöfer, M. Mondeshki and W. Tremel, *Nanoscale*, 2021, **13**, 8146–8162.
14 X.-J. Huang, J. Bao, Y. Han, C.-W. Cui, J.-X. Wang, X.-F. Zeng and J.-F. Chen, *J. Mater. Chem. C*, 2018, **6**, 7783–7789.
15 B.-T. Liu, T.-Y. Hung, N. E. Gorji and A. H. Mosavi, *Results Phys.*, 2021, **29**, 104804.
16 J.-S. Lee, H.-C. Liu, G.-D. Peng and Y. Tseng, *J. Cryst. Growth*, 2017, **465**, 27–33.
17 C. Guo, S. Yin, Q. Dong and T. Sato, *CrystEngComm*, 2012, **14**, 7727–7732.
18 T. Wang, Y. Xiong, R. Li and H. Cai, *New J. Chem.*, 2016, **40**, 7476–7481.
19 J. Choi, K. Moon, I. Kang, S. Kim, P. J. Yoo, K. W. Oh and J. Park, *Chem. Eng. J.*, 2015, **281**, 236–242.
20 L. Tegg, D. Cuskelly and V. J. Keast, *Plasmonics*, 2018, **13**, 437–444.
21 C. Guo, S. Yin, Q. Dong and T. Sato, *Nanoscale*, 2012, **4**, 3394–3398.
22 M. Yan, H. Gu, Z. Liu, C. Guo and S. Liu, *RSC Adv.*, 2015, **5**, 967–973.
23 P. Zavalij, J. Guo, M. S. Whittingham, R. A. Jacobson, V. Pecharsky, C. K. Bucher and S.-J. Hwu, *J. Solid State Chem.*, 1996, **123**, 83–92.
24 K. Manthiram and A. P. Alivisatos, *J. Am. Chem. Soc.*, 2012, **134**, 3995–3998.
25 S. Nakakura, A. F. Arif, K. Machida, K. Adachi and T. Ogi, *Inorg. Chem.*, 2019, **58**, 9101–9107.
26 T. Berestok, P. Guardia, J. Blanco, R. Nafria, P. Torruella, L. López-Conesa, S. Estradé, M. Ibáñez, J. de Roo, Z. Luo, D. Cadavid, J. C. Martins, M. V. Kovalenko, F. Peiró and A. Cabot, *Chem. Mater.*, 2017, **29**, 4418–4424.
27 M. Calcabrini, D. Van den Eynden, S. S. Ribot, R. Pokratath, J. Llorca, J. De Roo and M. Ibáñez, *JACS Au*, 2021, **1**, 1898–1903.
28 Y. Tang, M. Liang, M. Zhang, A. Honarfar, X. Zou, M. Abdellah, T. Pullerits, K. Zheng and Q. Chi, *ACS Appl. Mater. Interfaces*, 2020, **12**, 858–867.
29 Y. Xin, W. Shen, Z. Deng and J. Zhang, *ACS Appl. Mater. Interfaces*, 2018, **10**, 28971–28978.
30 D. Wilson and M. A. Langell, *Appl. Surf. Sci.*, 2014, **303**, 6–13.
31 M. Aslam, E. A. Schultz, T. Sun, T. Meade and V. P. Dravid, *Cryst. Growth Des.*, 2007, **7**, 471–475.
32 P. Giannozzi, O. Andreussi, T. Brumme, O. Bunau, M. Buongiorno Nardelli, M. Calandra, R. Car, C. Cavazzoni, D. Ceresoli, M. Cococcioni, *et al.*, *J. Phys.: Condens. Matter*, 2017, **29**, 465901.
33 M. Walter, M. Moseler and L. Pastewka, *Phys. Rev. B*, 2016, **94**, 041112.
34 S. Yoshio and K. Adachi, *Mater. Res. Express*, 2019, **6**, 026548.
35 J. Kim, B. J. Murdoch, J. G. Partridge, K. Xing, D.-C. Qi, J. Lipton-Duffin, C. F. McConville, J. van Embden and E. D. Gaspera, *Adv. Mater. Interfaces*, 2020, **7**, 2000655.
36 J. I. Scott, R. F. Martinez-Gazoni, M. W. Allen and R. J. Reeves, *J. Appl. Phys.*, 2019, **126**, 135702.
37 E. Della Gaspera, A. S. R. Chesman, J. van Embden and J. J. Jasieniak, *ACS Nano*, 2014, **8**, 9154–9163.
38 T. J. Davis and D. E. Gómez, *Rev. Mod. Phys.*, 2017, **89**, 011003.

